

Ξ'_c Production at *BABAR*

The *BABAR* Collaboration

September 17, 2018

Abstract

Using 232 fb^{-1} of data collected by the *BABAR* detector, the $\Xi'_c{}^+$ and $\Xi'_c{}^0$ baryons are reconstructed through the decays: $\Xi'_c{}^+ \rightarrow \Xi_c{}^+ \gamma$ and $\Xi'_c{}^0 \rightarrow \Xi_c{}^0 \gamma$, where $\Xi_c{}^+ \rightarrow \Xi^- \pi^+ \pi^+$ and $\Xi_c{}^0 \rightarrow \Xi^- \pi^+$. By measuring the efficiency-corrected yields in different intervals of the center-of-mass momentum, the production rates from B decays and from the continuum are extracted. For production from B decays, the branching fractions are found to be $\mathcal{B}(B \rightarrow \Xi'_c{}^+ X) \times \mathcal{B}(\Xi_c{}^+ \rightarrow \Xi^- \pi^+ \pi^+) = [1.69 \pm 0.17 \text{ (exp.)} \pm 0.10 \text{ (model)}] \times 10^{-4}$ and $\mathcal{B}(B \rightarrow \Xi'_c{}^0 X) \times \mathcal{B}(\Xi_c{}^0 \rightarrow \Xi^- \pi^+) = [0.67 \pm 0.07 \text{ (exp.)} \pm 0.03 \text{ (model)}] \times 10^{-4}$. For production from the continuum the cross-sections are found to be $\sigma(e^+ e^- \rightarrow \Xi'_c{}^+ X) \times \mathcal{B}(\Xi_c{}^+ \rightarrow \Xi^- \pi^+ \pi^+) = 141 \pm 24 \text{ (exp.)} \pm 19 \text{ (model) fb}$ and $\sigma(e^+ e^- \rightarrow \Xi'_c{}^0 X) \times \mathcal{B}(\Xi_c{}^0 \rightarrow \Xi^- \pi^+) = 70 \pm 11 \text{ (exp.)} \pm 6 \text{ (model) fb}$. The helicity angle distributions of Ξ'_c decays are studied and found to be consistent with $J = \frac{1}{2}$.

Submitted to the 33rd International Conference on High-Energy Physics, ICHEP 06,
26 July—2 August 2006, Moscow, Russia.

Stanford Linear Accelerator Center, Stanford University, Stanford, CA 94309

Work supported in part by Department of Energy contract DE-AC03-76SF00515.

The BABAR Collaboration,

B. Aubert, R. Barate, M. Bona, D. Boutigny, F. Couderc, Y. Karyotakis, J. P. Lees, V. Poireau,
V. Tisserand, A. Zghiche

*Laboratoire de Physique des Particules, IN2P3/CNRS et Université de Savoie, F-74941 Annecy-Le-Vieux,
France*

E. Grauges

Universitat de Barcelona, Facultat de Física, Departament ECM, E-08028 Barcelona, Spain

A. Palano

Università di Bari, Dipartimento di Fisica and INFN, I-70126 Bari, Italy

J. C. Chen, N. D. Qi, G. Rong, P. Wang, Y. S. Zhu

Institute of High Energy Physics, Beijing 100039, China

G. Eigen, I. Ofte, B. Stugu

University of Bergen, Institute of Physics, N-5007 Bergen, Norway

G. S. Abrams, M. Battaglia, D. N. Brown, J. Button-Shafer, R. N. Cahn, E. Charles, M. S. Gill,
Y. Groysman, R. G. Jacobsen, J. A. Kadyk, L. T. Kerth, Yu. G. Kolomensky, G. Kukartsev, G. Lynch,
L. M. Mir, T. J. Orimoto, M. Pripstein, N. A. Roe, M. T. Ronan, W. A. Wenzel

Lawrence Berkeley National Laboratory and University of California, Berkeley, California 94720, USA

P. del Amo Sanchez, M. Barrett, K. E. Ford, A. J. Hart, T. J. Harrison, C. M. Hawkes, S. E. Morgan,
A. T. Watson

University of Birmingham, Birmingham, B15 2TT, United Kingdom

T. Held, H. Koch, B. Lewandowski, M. Pelizaeus, K. Peters, T. Schroeder, M. Steinke
Ruhr Universität Bochum, Institut für Experimentalphysik 1, D-44780 Bochum, Germany

J. T. Boyd, J. P. Burke, W. N. Cottingham, D. Walker

University of Bristol, Bristol BS8 1TL, United Kingdom

D. J. Asgeirsson, T. Cuhadar-Donszelmann, B. G. Fulsom, C. Hearty, N. S. Knecht, T. S. Mattison,
J. A. McKenna

University of British Columbia, Vancouver, British Columbia, Canada V6T 1Z1

A. Khan, P. Kyberd, M. Saleem, D. J. Sherwood, L. Teodorescu

Brunel University, Uxbridge, Middlesex UB8 3PH, United Kingdom

V. E. Blinov, A. D. Bukin, V. P. Druzhinin, V. B. Golubev, A. P. Onuchin, S. I. Serednyakov,
Yu. I. Skovpen, E. P. Solodov, K. Yu Todyshev

Budker Institute of Nuclear Physics, Novosibirsk 630090, Russia

D. S. Best, M. Bondioli, M. Bruinsma, M. Chao, S. Curry, I. Eschrich, D. Kirkby, A. J. Lankford, P. Lund,
M. Mandelkern, R. K. Mommsen, W. Roethel, D. P. Stoker

University of California at Irvine, Irvine, California 92697, USA

S. Abachi, C. Buchanan

University of California at Los Angeles, Los Angeles, California 90024, USA

S. D. Foulkes, J. W. Gary, O. Long, B. C. Shen, K. Wang, L. Zhang
University of California at Riverside, Riverside, California 92521, USA

H. K. Hadavand, E. J. Hill, H. P. Paar, S. Rahatlou, V. Sharma
University of California at San Diego, La Jolla, California 92093, USA

J. W. Berryhill, C. Campagnari, A. Cunha, B. Dahmes, T. M. Hong, D. Kovalskyi, J. D. Richman
University of California at Santa Barbara, Santa Barbara, California 93106, USA

T. W. Beck, A. M. Eisner, C. J. Flacco, C. A. Heusch, J. Kroseberg, W. S. Lockman, G. Nesom, T. Schalk,
B. A. Schumm, A. Seiden, P. Spradlin, D. C. Williams, M. G. Wilson
University of California at Santa Cruz, Institute for Particle Physics, Santa Cruz, California 95064, USA

J. Albert, E. Chen, A. Dvoretzkii, F. Fang, D. G. Hitlin, I. Narsky, T. Piatenko, F. C. Porter, A. Ryd,
A. Samuel
California Institute of Technology, Pasadena, California 91125, USA

G. Mancinelli, B. T. Meadows, K. Mishra, M. D. Sokoloff
University of Cincinnati, Cincinnati, Ohio 45221, USA

F. Blanc, P. C. Bloom, S. Chen, W. T. Ford, J. F. Hirschauer, A. Kreisel, M. Nagel, U. Nauenberg,
A. Olivas, W. O. Ruddick, J. G. Smith, K. A. Ulmer, S. R. Wagner, J. Zhang
University of Colorado, Boulder, Colorado 80309, USA

A. Chen, E. A. Eckhart, A. Soffer, W. H. Toki, R. J. Wilson, F. Winklmeier, Q. Zeng
Colorado State University, Fort Collins, Colorado 80523, USA

D. D. Altenburg, E. Feltresi, A. Hauke, H. Jasper, J. Merkel, A. Petzold, B. Spaan
Universität Dortmund, Institut für Physik, D-44221 Dortmund, Germany

T. Brandt, V. Klose, H. M. Lacker, W. F. Mader, R. Nogowski, J. Schubert, K. R. Schubert, R. Schwierz,
J. E. Sundermann, A. Volk
Technische Universität Dresden, Institut für Kern- und Teilchenphysik, D-01062 Dresden, Germany

D. Bernard, G. R. Bonneaud, E. Latour, Ch. Thiebaux, M. Verderi
Laboratoire Leprince-Ringuet, CNRS/IN2P3, Ecole Polytechnique, F-91128 Palaiseau, France

P. J. Clark, W. Gradl, F. Muheim, S. Playfer, A. I. Robertson, Y. Xie
University of Edinburgh, Edinburgh EH9 3JZ, United Kingdom

M. Andreotti, D. Bettoni, C. Bozzi, R. Calabrese, G. Cibinetto, E. Luppi, M. Negrini, A. Petrella,
L. Piemontese, E. Prencipe
Università di Ferrara, Dipartimento di Fisica and INFN, I-44100 Ferrara, Italy

F. Anulli, R. Baldini-Ferroli, A. Calcaterra, R. de Sangro, G. Finocchiaro, S. Pacetti, P. Patteri,
I. M. Peruzzi,¹ M. Piccolo, M. Rama, A. Zallo
Laboratori Nazionali di Frascati dell'INFN, I-00044 Frascati, Italy

¹Also with Università di Perugia, Dipartimento di Fisica, Perugia, Italy

A. Buzzo, R. Capra, R. Contri, M. Lo Vetere, M. M. Macri, M. R. Monge, S. Passaggio, C. Patrignani,
E. Robutti, A. Santroni, S. Tosi

Università di Genova, Dipartimento di Fisica and INFN, I-16146 Genova, Italy

G. Brandenburg, K. S. Chaisanguanthum, M. Morii, J. Wu

Harvard University, Cambridge, Massachusetts 02138, USA

R. S. Dubitzky, J. Marks, S. Schenk, U. Uwer

Universität Heidelberg, Physikalisches Institut, Philosophenweg 12, D-69120 Heidelberg, Germany

D. J. Bard, W. Bhimji, D. A. Bowerman, P. D. Dauncey, U. Egede, R. L. Flack, J. A. Nash,
M. B. Nikolich, W. Panduro Vazquez

Imperial College London, London, SW7 2AZ, United Kingdom

P. K. Behera, X. Chai, M. J. Charles, U. Mallik, N. T. Meyer, V. Ziegler

University of Iowa, Iowa City, Iowa 52242, USA

J. Cochran, H. B. Crawley, L. Dong, V. Eyges, W. T. Meyer, S. Prell, E. I. Rosenberg, A. E. Rubin

Iowa State University, Ames, Iowa 50011-3160, USA

A. V. Gritsan

Johns Hopkins University, Baltimore, Maryland 21218, USA

A. G. Denig, M. Fritsch, G. Schott

Universität Karlsruhe, Institut für Experimentelle Kernphysik, D-76021 Karlsruhe, Germany

N. Arnaud, M. Davier, G. Grosdidier, A. Höcker, F. Le Diberder, V. Lepeltier, A. M. Lutz, A. Oyanguren,
S. Pruvot, S. Rodier, P. Roudeau, M. H. Schune, A. Stocchi, W. F. Wang, G. Wormser

*Laboratoire de l'Accélérateur Linéaire, IN2P3/CNRS et Université Paris-Sud 11, Centre Scientifique
d'Orsay, B.P. 34, F-91898 ORSAY Cedex, France*

C. H. Cheng, D. J. Lange, D. M. Wright

Lawrence Livermore National Laboratory, Livermore, California 94550, USA

C. A. Chavez, I. J. Forster, J. R. Fry, E. Gabathuler, R. Gamet, K. A. George, D. E. Hutchcroft,
D. J. Payne, K. C. Schofield, C. Touramanis

University of Liverpool, Liverpool L69 7ZE, United Kingdom

A. J. Bevan, F. Di Lodovico, W. Menges, R. Sacco

Queen Mary, University of London, E1 4NS, United Kingdom

G. Cowan, H. U. Flaecher, D. A. Hopkins, P. S. Jackson, T. R. McMahon, S. Ricciardi, F. Salvatore,
A. C. Wren

*University of London, Royal Holloway and Bedford New College, Egham, Surrey TW20 0EX, United
Kingdom*

D. N. Brown, C. L. Davis

University of Louisville, Louisville, Kentucky 40292, USA

J. Allison, N. R. Barlow, R. J. Barlow, Y. M. Chia, C. L. Edgar, G. D. Lafferty, M. T. Naisbit,
J. C. Williams, J. I. Yi

University of Manchester, Manchester M13 9PL, United Kingdom

C. Chen, W. D. Hulsbergen, A. Jawahery, C. K. Lae, D. A. Roberts, G. Simi

University of Maryland, College Park, Maryland 20742, USA

G. Blaylock, C. Dallapiccola, S. S. Hertzbach, X. Li, T. B. Moore, S. Saremi, H. Staengle

University of Massachusetts, Amherst, Massachusetts 01003, USA

R. Cowan, G. Sciolla, S. J. Sekula, M. Spitznagel, F. Taylor, R. K. Yamamoto

*Massachusetts Institute of Technology, Laboratory for Nuclear Science, Cambridge, Massachusetts 02139,
USA*

H. Kim, S. E. McLachlin, P. M. Patel, S. H. Robertson

McGill University, Montréal, Québec, Canada H3A 2T8

A. Lazzaro, V. Lombardo, F. Palombo

Università di Milano, Dipartimento di Fisica and INFN, I-20133 Milano, Italy

J. M. Bauer, L. Cremaldi, V. Eschenburg, R. Godang, R. Kroeger, D. A. Sanders, D. J. Summers,
H. W. Zhao

University of Mississippi, University, Mississippi 38677, USA

S. Brunet, D. Côté, M. Simard, P. Taras, F. B. Viaud

Université de Montréal, Physique des Particules, Montréal, Québec, Canada H3C 3J7

H. Nicholson

Mount Holyoke College, South Hadley, Massachusetts 01075, USA

N. Cavallo,² G. De Nardo, F. Fabozzi,³ C. Gatto, L. Lista, D. Monorchio, P. Paolucci, D. Piccolo,
C. Sciacca

Università di Napoli Federico II, Dipartimento di Scienze Fisiche and INFN, I-80126, Napoli, Italy

M. A. Baak, G. Raven, H. L. Snoek

*NIKHEF, National Institute for Nuclear Physics and High Energy Physics, NL-1009 DB Amsterdam, The
Netherlands*

C. P. Jessop, J. M. LoSecco

University of Notre Dame, Notre Dame, Indiana 46556, USA

T. Allmendinger, G. Benelli, L. A. Corwin, K. K. Gan, K. Honscheid, D. Hufnagel, P. D. Jackson,
H. Kagan, R. Kass, A. M. Rahimi, J. J. Regensburger, R. Ter-Antonyan, Q. K. Wong

Ohio State University, Columbus, Ohio 43210, USA

N. L. Blount, J. Brau, R. Frey, O. Igonkina, J. A. Kolb, M. Lu, R. Rahmat, N. B. Sinev, D. Strom,
J. Strube, E. Torrence

University of Oregon, Eugene, Oregon 97403, USA

²Also with Università della Basilicata, Potenza, Italy

³Also with Università della Basilicata, Potenza, Italy

A. Gaz, M. Margoni, M. Morandin, A. Pompili, M. Posocco, M. Rotondo, F. Simonetto, R. Stroili, C. Voci
Università di Padova, Dipartimento di Fisica and INFN, I-35131 Padova, Italy

M. Benayoun, H. Briand, J. Chauveau, P. David, L. Del Buono, Ch. de la Vaissière, O. Hamon,
B. L. Hartfiel, M. J. J. John, Ph. Leruste, J. Malcès, J. Ocariz, L. Roos, G. Therin
*Laboratoire de Physique Nucléaire et de Hautes Energies, IN2P3/CNRS, Université Pierre et Marie
Curie-Paris6, Université Denis Diderot-Paris7, F-75252 Paris, France*

L. Gladney, J. Panetta
University of Pennsylvania, Philadelphia, Pennsylvania 19104, USA

M. Biasini, R. Covarelli
Università di Perugia, Dipartimento di Fisica and INFN, I-06100 Perugia, Italy

C. Angelini, G. Batignani, S. Bettarini, F. Bucci, G. Calderini, M. Carpinelli, R. Cenci, F. Forti,
M. A. Giorgi, A. Lusiani, G. Marchiori, M. A. Mazur, M. Morganti, N. Neri, E. Paoloni, G. Rizzo,
J. J. Walsh
Università di Pisa, Dipartimento di Fisica, Scuola Normale Superiore and INFN, I-56127 Pisa, Italy

M. Haire, D. Judd, D. E. Wagoner
Prairie View A&M University, Prairie View, Texas 77446, USA

J. Biesiada, N. Danielson, P. Elmer, Y. P. Lau, C. Lu, J. Olsen, A. J. S. Smith, A. V. Telnov
Princeton University, Princeton, New Jersey 08544, USA

F. Bellini, G. Cavoto, A. D’Orazio, D. del Re, E. Di Marco, R. Faccini, F. Ferrarotto, F. Ferroni,
M. Gaspero, L. Li Gioi, M. A. Mazzoni, S. Morganti, G. Piredda, F. Polci, F. Safai Tehrani, C. Voena
Università di Roma La Sapienza, Dipartimento di Fisica and INFN, I-00185 Roma, Italy

M. Ebert, H. Schröder, R. Waldi
Universität Rostock, D-18051 Rostock, Germany

T. Adye, N. De Groot, B. Franek, E. O. Olaiya, F. F. Wilson
Rutherford Appleton Laboratory, Chilton, Didcot, Oxon, OX11 0QX, United Kingdom

R. Aleksan, S. Emery, A. Gaidot, S. F. Ganzhur, G. Hamel de Monchenault, W. Kozanecki, M. Legendre,
G. Vasseur, Ch. Yèche, M. Zito
DSM/Daphnia, CEA/Saclay, F-91191 Gif-sur-Yvette, France

X. R. Chen, H. Liu, W. Park, M. V. Purohit, J. R. Wilson
University of South Carolina, Columbia, South Carolina 29208, USA

M. T. Allen, D. Aston, R. Bartoldus, P. Bechtle, N. Berger, R. Claus, J. P. Coleman, M. R. Convery,
M. Cristinziani, J. C. Dingfelder, J. Dorfan, G. P. Dubois-Felsmann, D. Dujmic, W. Dunwoodie,
R. C. Field, T. Glanzman, S. J. Gowdy, M. T. Graham, P. Grenier,⁴ V. Halyo, C. Hast, T. Hryn’ova,
W. R. Innes, M. H. Kelsey, P. Kim, D. W. G. S. Leith, S. Li, S. Luitz, V. Luth, H. L. Lynch,
D. B. MacFarlane, H. Marsiske, R. Messner, D. R. Muller, C. P. O’Grady, V. E. Ozcan, A. Perazzo,
M. Perl, T. Pulliam, B. N. Ratcliff, A. Roodman, A. A. Salnikov, R. H. Schindler, J. Schwiening,
A. Snyder, J. Stelzer, D. Su, M. K. Sullivan, K. Suzuki, S. K. Swain, J. M. Thompson, J. Va’vra, N. van

⁴Also at Laboratoire de Physique Corpusculaire, Clermont-Ferrand, France

Bakel, M. Weaver, A. J. R. Weinstein, W. J. Wisniewski, M. Wittgen, D. H. Wright, A. K. Yarritu, K. Yi,
C. C. Young

Stanford Linear Accelerator Center, Stanford, California 94309, USA

P. R. Burchat, A. J. Edwards, S. A. Majewski, B. A. Petersen, C. Roat, L. Wilden

Stanford University, Stanford, California 94305-4060, USA

S. Ahmed, M. S. Alam, R. Bula, J. A. Ernst, V. Jain, B. Pan, M. A. Saeed, F. R. Wappler, S. B. Zain

State University of New York, Albany, New York 12222, USA

W. Bugg, M. Krishnamurthy, S. M. Spanier

University of Tennessee, Knoxville, Tennessee 37996, USA

R. Eckmann, J. L. Ritchie, A. Satpathy, C. J. Schilling, R. F. Schwitters

University of Texas at Austin, Austin, Texas 78712, USA

J. M. Izen, X. C. Lou, S. Ye

University of Texas at Dallas, Richardson, Texas 75083, USA

F. Bianchi, F. Gallo, D. Gamba

Università di Torino, Dipartimento di Fisica Sperimentale and INFN, I-10125 Torino, Italy

M. Bomben, L. Bosisio, C. Cartaro, F. Cossutti, G. Della Ricca, S. Dittongo, L. Lanceri, L. Vitale

Università di Trieste, Dipartimento di Fisica and INFN, I-34127 Trieste, Italy

V. Azzolini, N. Lopez-March, F. Martinez-Vidal

IFIC, Universitat de Valencia-CSIC, E-46071 Valencia, Spain

Sw. Banerjee, B. Bhuyan, C. M. Brown, D. Fortin, K. Hamano, R. Kowalewski, I. M. Nugent, J. M. Roney,
R. J. Sobie

University of Victoria, Victoria, British Columbia, Canada V8W 3P6

J. J. Back, P. F. Harrison, T. E. Latham, G. B. Mohanty, M. Pappagallo

Department of Physics, University of Warwick, Coventry CV4 7AL, United Kingdom

H. R. Band, X. Chen, B. Cheng, S. Dasu, M. Datta, K. T. Flood, J. J. Hollar, P. E. Kutter, B. Mellado,
A. Mihalyi, Y. Pan, M. Pierini, R. Prepost, S. L. Wu, Z. Yu

University of Wisconsin, Madison, Wisconsin 53706, USA

H. Neal

Yale University, New Haven, Connecticut 06511, USA

1 INTRODUCTION

Charmed baryons have a complex and intricate spectroscopy. The states can be classified in the following categories:

State	Quark content	Isospin configuration
Λ_c	cud	Isosinglet
Σ_c	cqq	Isotriplet
Ξ_c	csq	Isodoublet
Ω_c	css	Isosinglet

where q indicates a u or a d quark. There are numerous states for each of these quark flavor configurations [1], several of which have been observed [2].

In this analysis, we focus on the Ξ_c states, and in particular on the lowest resonances above the ground state, the Ξ'_c . This is one of three Ξ_c states, listed below, which are not radially excited and which have zero orbital angular momentum:

State	Approx. mass (MeV/ c^2)	Light flavor wavefunction	J^P
Ξ_c	2470	Antisymmetric	$\frac{1}{2}^+$
Ξ'_c	2580	Symmetric	$\frac{1}{2}^+$
Ξ_c^*	2645	Symmetric	$\frac{3}{2}^+$

Note that the J^P of the Ξ'_c and Ξ_c^* have not been directly measured but are assigned from the quark model predictions. In a recent study of the decay $\Xi_c^0 \rightarrow \Omega^- K^+$ [3], the helicity angle of the Ξ_c^0 was found to be consistent with $J = \frac{1}{2}$, though higher spins were not excluded.

The mass difference between the Ξ'_c and ground state is only $\Delta m \equiv m(\Xi'_c) - m(\Xi_c) \simeq 107$ MeV/ c^2 . Hence, the Ξ'_c is below threshold for a strong decay via $\Xi_c \pi$ or other final states such as $\Lambda_c \bar{K}$ or $D\Lambda$, and so it can only decay by photon emission, $\Xi'_c \rightarrow \Xi_c \gamma$.

The $\Xi_c^{'+}$ and $\Xi_c^{\prime 0}$ states were observed by CLEO in 5.0 fb^{-1} of data [4]. This observation has not yet been confirmed by another experiment. Charmed baryons can be produced in two ways at e^+e^- B -factories: from the continuum and in decays of B mesons. The CLEO measurement was made with requirements that $x_p \geq 0.5$ – 0.6 depending on the decay channel, where $x_p \equiv p^*/\sqrt{s/4 - m_{\Xi'_c}^2}$ and p^* is the center-of-mass momentum of the Ξ'_c . These requirements suppressed combinatorial background, but they also removed any Ξ'_c production from B -decays, retaining only the continuum production of Ξ'_c .

Recent results from *BABAR* and *Belle* indicate that B decays to charmed baryon pairs occur at a high rate even when the available phase space is small [5, 6, 7, 8, 9]. One possible explanation is that baryon formation is enhanced when the two baryons are almost at rest in their center-of-mass frame, and strongly suppressed when their relative motion is large (see Ref. [10] and the references therein). This may also explain threshold enhancements seen in several modes such as $B^- \rightarrow p\bar{p}K^-$ and $B^- \rightarrow p\bar{p}\bar{K}^0$ [11, 12]. If processes with low energy release are favored, the production of low-lying charmed baryon resonances such as Ξ'_c may be substantial. There is currently no experimental evidence for the production of Ξ'_c in B decays.

2 THE *BABAR* DETECTOR AND DATASET

The data used in this analysis were collected with the *BABAR* detector at the SLAC PEP-II asymmetric energy storage ring. A total of $(231.9 \pm 3.5) \text{ fb}^{-1}$ of data are used, of which 210.3 fb^{-1} were

taken on the $\Upsilon(4S)$ resonance ($\sqrt{s} = 10.58$ GeV) and the remaining 21.6 fb^{-1} were taken below the $B\bar{B}$ threshold ($\sqrt{s} = 10.54$ GeV). The on-resonance data contains $(228.3 \pm 2.5) \times 10^6 B\bar{B}$ pairs. The *BABAR* detector is described elsewhere [13].

Simulated events with Ξ'_c decaying into the desired final states are generated for the processes $e^+e^- \rightarrow c\bar{c} \rightarrow \Xi'_c X$ and $e^+e^- \rightarrow \Upsilon(4S) \rightarrow B\bar{B} \rightarrow \Xi'_c X$, where X represents the rest of the event. The *PYTHIA* simulation package [14], tuned to the global *BABAR* data, is used for the $c\bar{c}$ fragmentation and for B decays to Ξ'_c , and *GEANT4* [15] is used to simulate the detector response.

3 ANALYSIS METHOD

3.1 Overview

The $\Xi'_c{}^+$ and $\Xi'_c{}^0$ are reconstructed through the following decays:

$$\begin{aligned}\Xi'_c{}^+ &\rightarrow \Xi_c{}^+ \gamma \\ \Xi'_c{}^0 &\rightarrow \Xi_c{}^0 \gamma,\end{aligned}$$

where the daughter Ξ_c baryons are reconstructed as follows:

$$\begin{aligned}\Xi_c{}^+ &\rightarrow \Xi^- \pi^+ \pi^+ \\ \Xi_c{}^0 &\rightarrow \Xi^- \pi^+ \\ \Xi^- &\rightarrow \Lambda \pi^- \\ \Lambda &\rightarrow p \pi^-.\end{aligned}$$

The measured invariant mass spectra of the Ξ'_c candidates are corrected for efficiency. From the Ξ'_c yields in different p^* intervals, the production rates from B decays and from the continuum are extracted. We also study the helicity angle (θ_h) distribution.

3.2 Selection and reconstruction of Ξ_c^+ and Ξ_c^0

A Λ candidate is reconstructed by identifying a proton with dE/dx and Cherenkov angle measurements [13] and combining it with an oppositely charged track interpreted as a π^- , and fitting the tracks to a common vertex. The Λ candidate is then combined with a negatively charged track interpreted as a π^- , and fitted to a common vertex to form a Ξ^- candidate. For each Λ and Ξ^- , the invariant mass is required to be within 3σ of the central reconstructed value, where σ is the fitted mass resolution (approximately $1.0 \text{ MeV}/c^2$ for Λ and $1.5 \text{ MeV}/c^2$ for Ξ^-). The invariant mass is then constrained to the nominal value [2]. Each resulting Ξ^- candidate is then combined with one or two positively charged tracks interpreted as π^+ to form a Ξ_c^0 or Ξ_c^+ candidate. No mass constraint is applied to the Ξ_c candidates.

Since the Ξ^- has a long lifetime ($c\tau = 4.9$ cm), we improve the signal-to-background ratio by rejecting prompt background. The displacement vector from the event primary vertex to the Ξ^- decay vertex is required to be at least 2.5 mm in the plane transverse to the beam direction. In addition, the scalar product of the displacement vector with the Ξ^- momentum vector is required to be positive, rejecting unphysical candidates. These criteria were optimized in a previous analysis [7] and were finalized before the $m(\Xi_c\gamma)$ spectrum was examined in data.

The invariant mass distributions for the Ξ_c candidates satisfying these criteria are shown in Fig. 1. The fitted function (black curve) is the sum of two Gaussian functions with a common mean

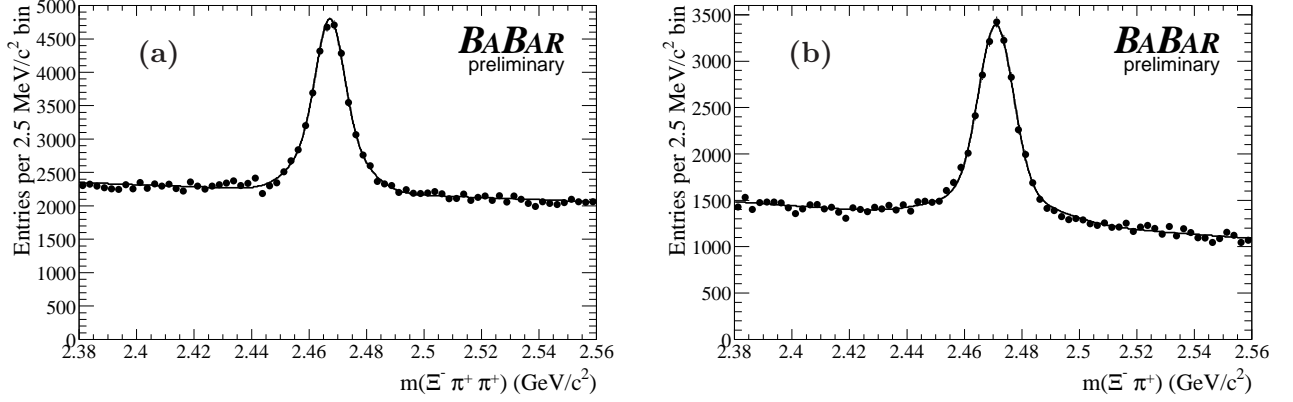


Figure 1: Invariant mass spectra of the Ξ_c ground states in 232 fb^{-1} of data. The reconstructed candidates of (a) Ξ_c^+ via $\Xi_c^+ \rightarrow \Xi^- \pi^+ \pi^+$, and (b) Ξ_c^0 via $\Xi_c^0 \rightarrow \Xi^- \pi^+$ are shown.

for the signal plus a first-order polynomial for the background. The half-widths at half-maximum (σ) of the signal lineshapes are $7.0 \text{ MeV}/c^2$ and $7.5 \text{ MeV}/c^2$ for Ξ_c^+ and Ξ_c^0 , respectively.

3.3 Reconstruction of $\Xi_c^{\prime+}$ and $\Xi_c^{\prime0}$

Clusters of energy in the electromagnetic calorimeter are identified. The cluster must spread over at least two crystals. Clusters which lie along the trajectory of a charged track in the event are eliminated. The remaining clusters define photon candidates. The energy of the photon candidate must be at least 30 MeV and the lateral moment (defined in Ref. [16]) must be less than 0.8. The Ξ_c candidates shown in Fig. 1 are then combined with each of the photon candidates to form Ξ_c' candidates. The mass difference Δm is then computed:

$$\Delta m = \begin{cases} m(\Xi^- \pi^+ \pi^+ \gamma) - m(\Xi^- \pi^+ \pi^+) & \text{for } \Xi_c^{\prime+} \\ m(\Xi^- \pi^+ \gamma) - m(\Xi^- \pi^+) & \text{for } \Xi_c^{\prime0} \end{cases}$$

Since Δm and $m(\Xi^- \pi^+ [\pi^+])$ are essentially uncorrelated and the mass difference between Ξ_c' and Ξ_c is small, this method gives good mass resolution and avoids the need to apply a mass-constraint to the Ξ_c candidates. To make the spectra easier to interpret, we plot the mass difference Δm plus a constant offset m_{offset} which is approximately equal to the nominal ground state mass; offsets of $2.467 \text{ GeV}/c^2$ and $2.471 \text{ GeV}/c^2$ are used for the Ξ_c^+ and Ξ_c^0 states, respectively. The spectra thus obtained are shown for Ξ_c^+ and Ξ_c^0 in Fig. 2. For each mode, the mass spectrum is shown for $p^* > 0.0 \text{ GeV}/c$ (upper), $p^* > 2.5 \text{ GeV}/c$ (middle), and $p^* > 3.5 \text{ GeV}/c$ (lower). Clear Ξ_c' signals are observed at a mass of approximately $2.58 \text{ GeV}/c^2$.

The photon selection criteria are quite loose, especially in comparison to the previous CLEO analysis which imposed a minimum photon energy of 100 MeV in addition to requirements on the lateral shower profile and a veto of photons from π^0 candidates. The reason for the different selection strategies is evident from a comparison of the energy spectra of photons from Ξ_c' produced in the continuum, Ξ_c' produced in B decays, and background (Fig. 3): the CLEO study excluded Ξ_c' from B decays and was optimized for sensitivity to continuum production of Ξ_c' where the photon energy is a powerful discriminant between signal and background, whereas the selection criteria for

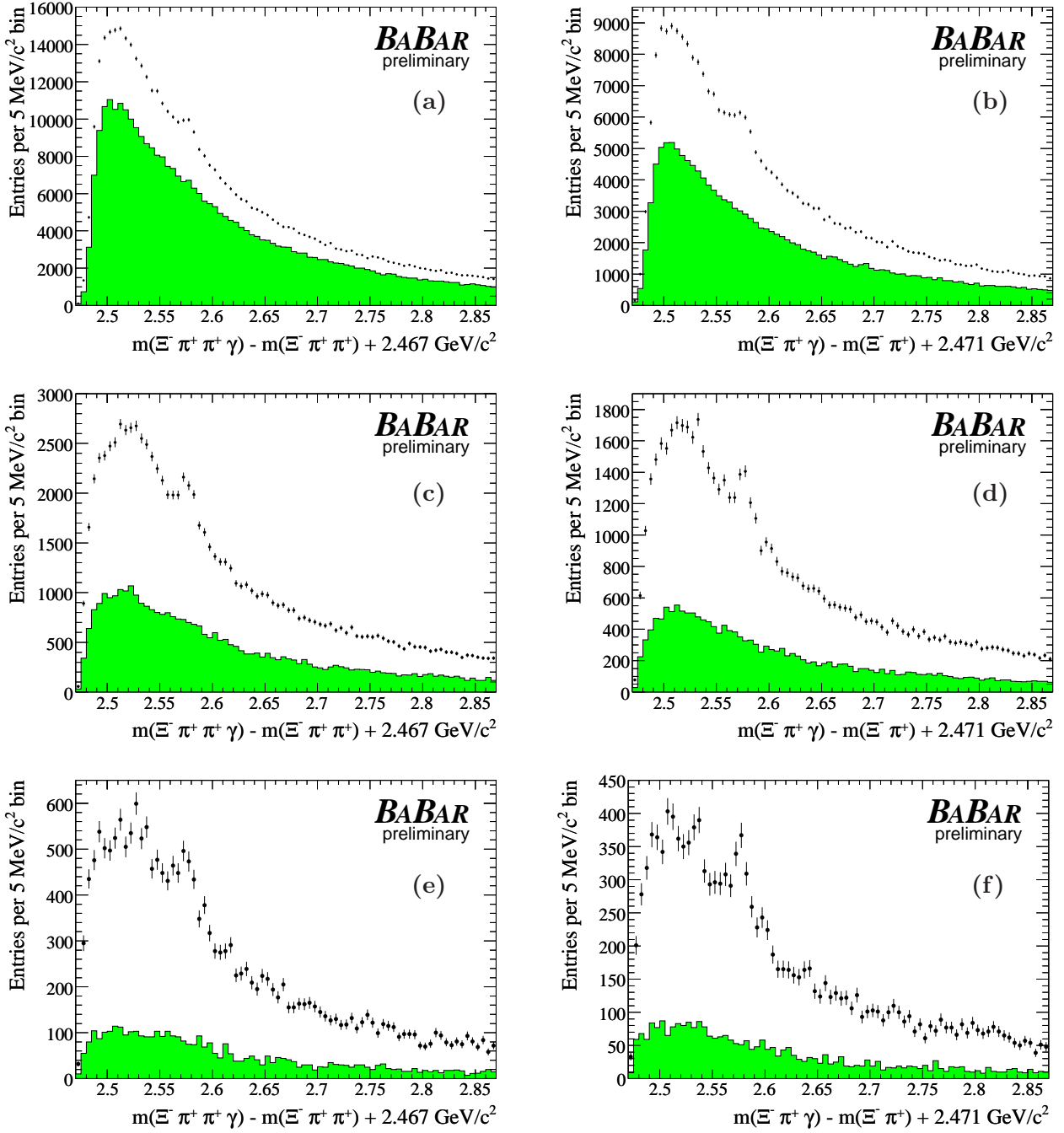


Figure 2: The $\Xi_c \gamma$ invariant mass spectra, shown with the following p^* requirements: 0.0 GeV/c (a,b), 2.5 GeV/c (c,d), 3.5 GeV/c (e,f). The left column shows $\Xi_c^+ \gamma$ and the right column shows $\Xi_c^0 \gamma$. The shaded histograms are taken from the Ξ_c mass sidebands ($5\sigma-8\sigma$ from the central value, where σ is the Ξ_c mass resolution), and the solid points are from the Ξ_c signal region (within 3σ of the central value).

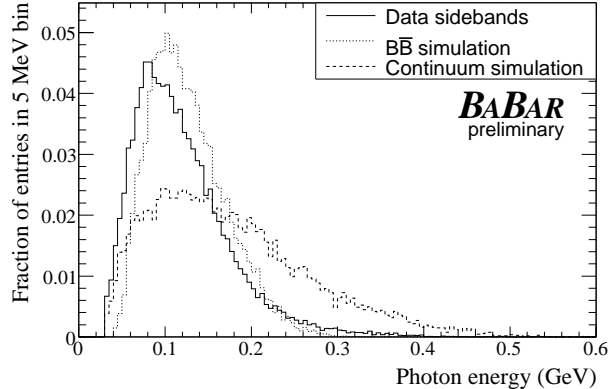


Figure 3: Photon energy distributions. The dotted and dashed histograms show photons from simulated Ξ'_c decays where the Ξ'_c is produced in B decays or from the continuum, respectively. The solid histogram shows photons from Ξ'_c candidates in the data with $m(\Xi^-\pi^+[\pi^+])$ in the Ξ_c mass sidebands and Δm in the signal region ($0.09 < \Delta m < 0.12$ GeV/ c^2).

this analysis were chosen to retain Ξ'_c from B decays with high efficiency. For illustrative purposes, the mass spectra of Ξ'_c candidates with tighter selection requirements are shown in Fig. 4.

3.4 Contributions to the invariant mass spectra

Four principal categories of events contribute to the Ξ'_c candidate distributions:

1. Signal $\Xi'_c \rightarrow \Xi_c \gamma$ decays which peak in both $m(\Xi^-\pi^+[\pi^+])$ and Δm . This is shown in Fig. 5 (a).
2. Combinatoric background which does not peak in either $m(\Xi^-\pi^+[\pi^+])$ or Δm . This is shown in Fig. 5 (b).
3. Background where a real Ξ_c is combined with an unrelated photon candidate. This peaks in $m(\Xi^-\pi^+[\pi^+])$ but not in Δm . This is shown in Fig. 5 (c).
4. Background contribution from events where a real $\Xi'_c \rightarrow \Xi_c \gamma$ decay occurs and the correct photon is found but the Ξ_c is partially mis-reconstructed. This is shown in Fig. 5 (d). This category generally does not peak in $m(\Xi^-\pi^+[\pi^+])$ but peaks in Δm (provided the momentum of the fake Ξ_c candidate is close to the real Ξ_c momentum).

Categories 2 and 3 do not peak in Δm , so we describe them with a smooth polynomial function. The Δm distribution of the fourth category is almost indistinguishable from the signal distribution.

One further possible contribution to the mass spectrum was considered: feed-down from the decay $\Xi_c^* \rightarrow \Xi_c \pi^0$ where only one of the two photons produced in the π^0 decay is used, leaving the same $\Xi_c \gamma$ final state as for a Ξ'_c decay. A study of this process with a simple kinematic simulation indicates that it would produce a very broad, non-peaking structure in the Ξ'_c mass spectrum, and therefore falls into the third category (Ξ_c background not peaking in Δm) already discussed.

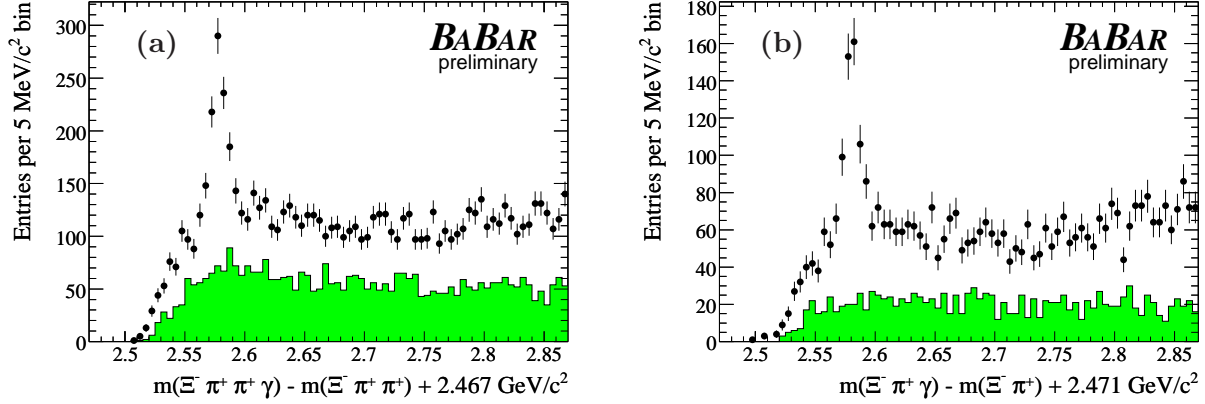


Figure 4: The $\Xi_c\gamma$ invariant mass spectra, requiring that $p^* > 2.5$ GeV/ c , that the photon energy be above 200 MeV, that the shower contain at least two crystals, that the lateral moment be less than 0.6, and that the shower be well-contained (shower energy within two cells of the maximum be at least 90% of the shower energy within one cell of the maximum). Plot (a) shows $\Xi_c^+\gamma$ and plot (b) shows $\Xi_c^0\gamma$. The mass windows are narrower than for Fig. 2: the shaded histograms are taken from the Ξ_c mass sidebands (5σ – 7σ from the central value) and the solid points are from the Ξ_c signal region (within 2σ of the central value).

3.5 Fitting procedure

The data are divided into ten p^* intervals of width 0.5 GeV/ c from 0.0 to 5.0 GeV/ c . For each p^* interval, the Δm distributions are fitted with the combination of a signal lineshape extracted from the simulated signal events and a second-order polynomial function to describe the background. The signal lineshape is parameterized as the sum of three Gaussian functions, parameters of which are determined from a fit to a high-statistics sample of simulated signal events in the corresponding p^* range. The lineshape is described in more detail in Section A.1 of Appendix A. During this fit all nine parameters of the triple Gaussian function are allowed to vary independently within fixed ranges.⁵ The lineshape is then fixed for fitting the data.

The fit to the data is performed in several steps:

1. First, we fit just the background function to an upper mass sideband of Ξ_c' , $2625 < \Delta m + m_{\text{offset}} < 2900$ MeV/ c^2 , using a binned maximum likelihood method. This provides the initial values of the background parameters.
2. Next, we attempt to fit the combined background and signal functions in the mass range 2550–2700 MeV/ c^2 . The signal mass and yield are floated, with the initial value of the signal yield set to zero. The background parameters are also left free; all other parameters are fixed. The mass is initially set to a central value extracted from a fit to the entire dataset and is allowed to vary within 10 MeV/ c^2 around this value. The fit uses a binned maximum likelihood method, followed by a binned χ^2 minimization with MINOS error-handling enabled [17].

⁵Fewer signal events were generated at the extremes of the p^* spectrum. In cases where fewer than 1,000 signal events were reconstructed, only two Gaussian functions were used. This applies to 0.0–0.5 GeV/ c for Ξ_c^+ , and to 4.0–4.5 GeV/ c for both Ξ_c^+ and Ξ_c^0 . For 4.5–5.0 GeV/ c no signal events were generated, so the fits of 4.0–4.5 GeV/ c were used.

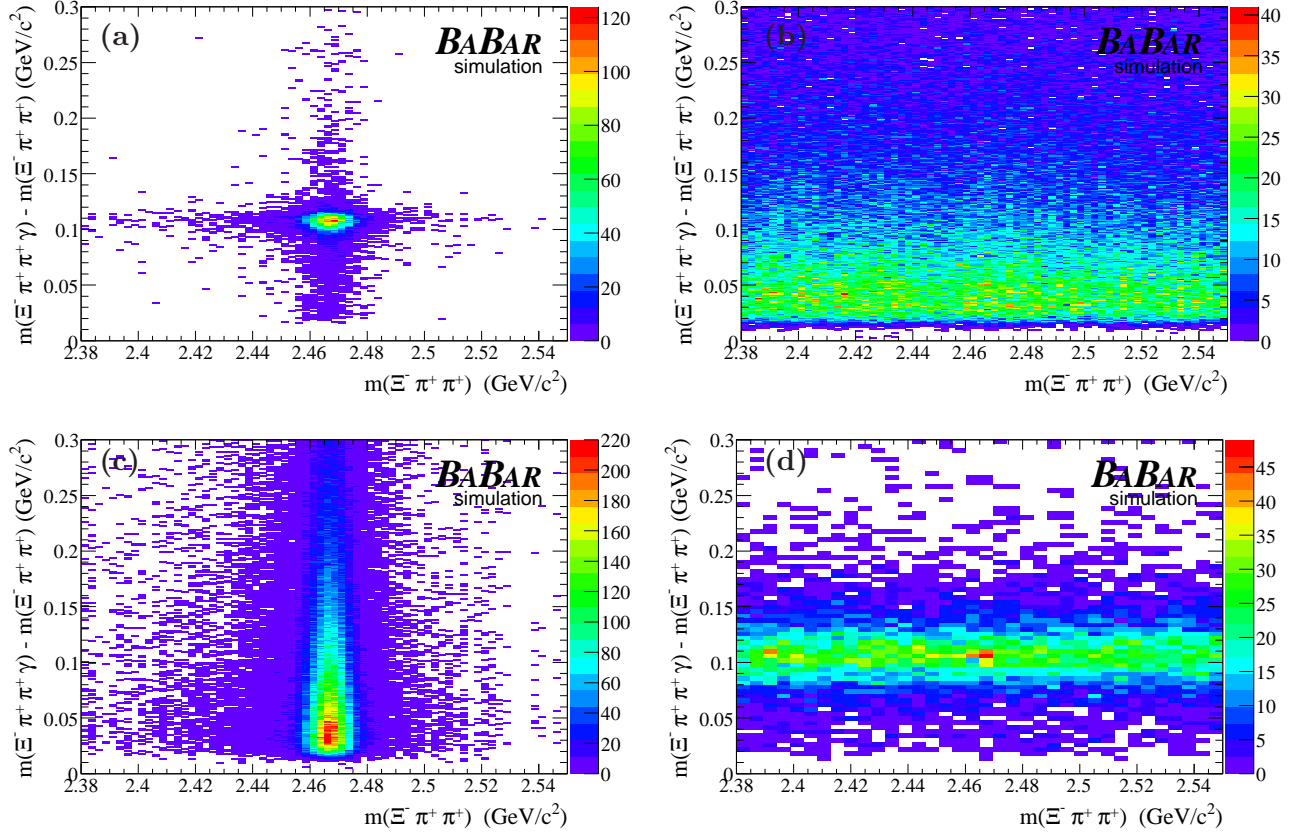


Figure 5: Illustrations of the signal and background contributions for $\Xi_c^0 \gamma$ in simulated continuum events. Plot (a) shows category 1, correctly reconstructed signal. Plot (b) shows category 2, combinatoric background. Plot (c) shows category 3, background with real Ξ_c . Plot (d) shows category 4, where a photon from a real Ξ_c' decay is combined with an incorrectly reconstructed Ξ_c .

3. We then check whether the fit converges to a physical value. If the signal mass is within $2 \text{ MeV}/c^2$ of the edge of the allowed range or the yield is unphysical (above 50,000 or below -100), we reject the fit. This typically occurs when studying a region of phase space where the signal yield is too small to fit with a floating mass.
4. If the first fit is rejected, we reset the parameters to the initial values described in step 2 and fix the mass to the central value extracted from the fit to the entire dataset. The fit is then repeated.

The individual fitted spectra are shown in Appendix B.

To remove the category 4 background described in Section 3.4, we perform a sideband subtraction in $m(\Xi^- \pi^+ [\pi^+])$ as follows:

- The Δm distribution of events in the Ξ_c mass signal region $-3\sigma < m(\Xi^- \pi^+ [\pi^+]) - m_0 < +3\sigma$ is plotted, where σ is the Ξ_c mass resolution and m_0 is the central value of the Ξ_c mass peak.
- Similarly, the Δm distribution for events in the Ξ_c mass sidebands, $5\sigma < |m(\Xi^- \pi^+ [\pi^+]) - m_0| < 8\sigma$, is plotted.
- The Δm distributions are fitted with a signal lineshape plus a polynomial background as described above. The integral of the signal function gives the combined yields of events from categories 1 and 4 in that $m(\Xi^- \pi^+ [\pi^+])$ range.
- The fitted yield from the sidebands is subtracted from the fitted yield in the signal region.

This process suppresses the category 4 background but retains the signal with high efficiency ($\sim 95\%$ at low p^* and $\sim 90\%$ at high p^*). A small fraction of category 4 events have peaking structure in $m(\Xi^- \pi^+ [\pi^+])$ and survive the sideband subtraction; this rate is 1% or less of the category 1 rate in all cases so we neglect it.

After performing the sideband subtraction described above, the numbers of background-subtracted $\Xi_c'^+$ and $\Xi_c'^0$ are 3341 ± 375 and 3195 ± 301 , respectively. The p^* distributions are shown in Fig. 6. As discussed in Section 1, there are two contributions: Ξ_c' from B decays and from the continuum. Ξ_c' produced in B decays have low momentum, especially if the recoiling antibaryon is also charmed. Allowing for the motion of the B mesons, the kinematic limit is $p^* < 2.08 \text{ GeV}/c$, but this corresponds to the process $\bar{B} \rightarrow \Xi_c' \bar{p}$ which is heavily suppressed. The limit for Cabibbo-allowed processes is $p^* < 2.02 \text{ GeV}/c$. By contrast, continuum production occurs mainly at higher values of p^* , with a kinematic limit of $p^* < 4.63 \text{ GeV}/c$ at $\sqrt{s} = 10.6 \text{ GeV}$. Two separate peaks corresponding to these processes are clearly visible in Fig. 6.

3.6 Efficiency correction

For each p^* interval, the efficiency ε is determined from simulated events in the corresponding p^* range:

$$\varepsilon = \frac{\text{Yield of true } \Xi_c' \text{ in } m(\Xi^- \pi^+ [\pi^+]) \text{ signal window}}{\text{Number of generated } \Xi_c'}, \quad (1)$$

where the yield is obtained by fitting the Δm spectrum and true Ξ_c' are identified with MC generator information. An additional correction is made to take into account signal events which fall into the $m(\Xi^- \pi^+ [\pi^+])$ sidebands and are subtracted from the yield as described in Section 3.5. This

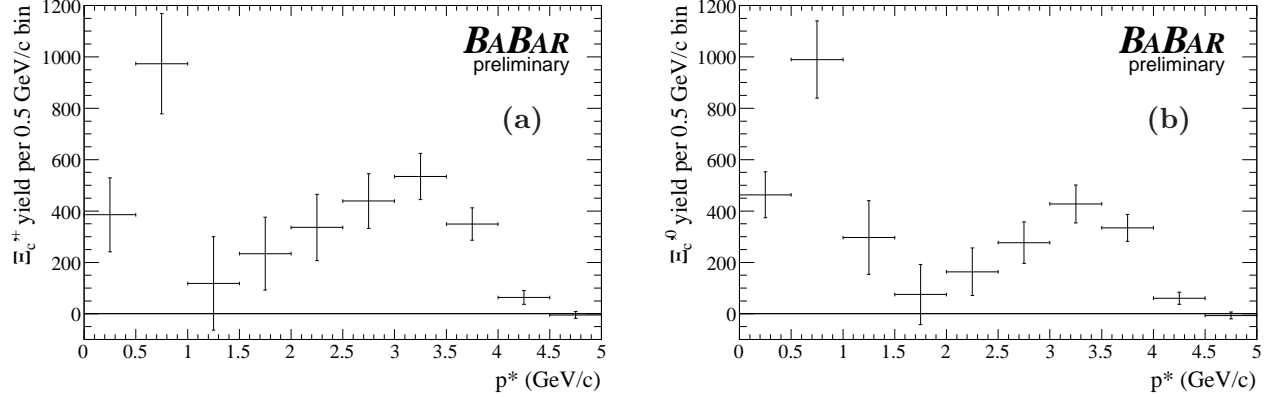


Figure 6: Background-subtracted Ξ_c momentum spectra, not corrected for efficiency. The yield in each p^* interval is shown for (a) $\Xi_c'^+$ and (b) $\Xi_c'^0$.

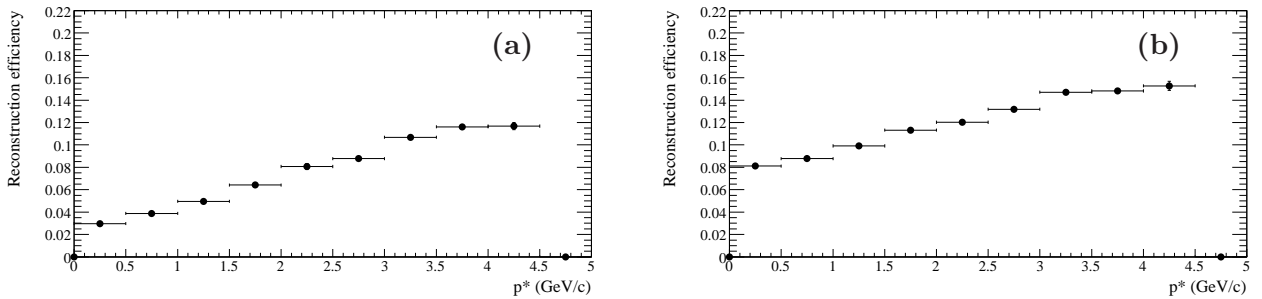


Figure 7: Efficiency as a function of p^* for (a) $\Xi_c'^+$ and (b) $\Xi_c'^0$. The factor $\mathcal{B}(\Lambda \rightarrow p\pi^-)$ is not included.

correction, $\delta\varepsilon$, is obtained from the $m(\Xi^- \pi^+ [\pi^+])$ lineshape of simulated Ξ_c' in the relevant p^* range:

$$\delta\varepsilon = \frac{\text{Yield of true } \Xi_c' \text{ in } m(\Xi^- \pi^+ [\pi^+]) \text{ sideband}}{\text{Yield of true } \Xi_c' \text{ in } m(\Xi^- \pi^+ [\pi^+]) \text{ signal window}}. \quad (2)$$

This is a small effect (approximately 1% for Ξ_c' produced in B decays and 2% for Ξ_c' produced from the continuum). The overall efficiency, $\varepsilon(1 - \delta\varepsilon)$, is shown in Fig. 7.

4 SYSTEMATIC STUDIES

The following systematic effects are considered. The first four are applied only to the overall normalization; the others are treated as fully uncorrelated and are applied to each p^* interval separately. All uncertainties quoted are relative.

Particle identification: A systematic uncertainty of 3.5% is assigned to the efficiency of the proton identification, as in a previous analysis of the Ξ_c system [7].

Tracking efficiency: To correct for a known discrepancy in tracking efficiency between data and simulation, systematic corrections of $(2.35 \pm 7.0)\%$ and $(1.55 \pm 5.6)\%$ are applied to the efficiency for reconstruction of $\Xi_c^+ \rightarrow \Xi^- \pi^+ \pi^+$ and $\Xi_c^0 \rightarrow \Xi^- \pi^+$, respectively.

Photon efficiency: Based on studies of photon-finding efficiency in control samples, a systematic uncertainty of 1.8% is applied to the efficiency.

Λ branching fraction: The world-average branching fraction is $\mathcal{B}(\Lambda \rightarrow p\pi^-) = (63.9 \pm 0.5)\%$. This results in a 0.8% systematic uncertainty.

Finite simulation statistics: The statistical uncertainty in the efficiency calculation in each p^* interval is applied as a systematic uncertainty to the specific data point. This is 5% or lower in each interval.

Signal fitting procedure: The analysis is repeated with a different functional form for the signal lineshape, described in Section A.2 of Appendix A. For each p^* interval, the systematic uncertainty is taken to be the difference between the efficiency-corrected yields from the two functional forms divided by $\sqrt{2}$. The value depends on the specific p^* interval, but is typically around 5–10%.

Background fitting procedure: The background shape is changed from a second-order polynomial to a fourth-order polynomial and the fit range is increased substantially. For each p^* interval, the systematic uncertainty is taken to be the difference between the efficiency-corrected yields from the two methods divided by $\sqrt{2}$. This varies between p^* intervals, but is typically around 5–10%. In a few intervals with low yields it rises to 30–50%, but is always lower than the statistical uncertainty.

Efficiency correction within a p^* interval: If the simulation does not correctly model the p^* distribution within a p^* interval and the efficiency varies significantly across that interval, the efficiency may not be predicted correctly. This effect was studied in a previous analysis and found to be a few percent or less with the *BABAR* simulation [7]. We assign a systematic uncertainty of 4% for each p^* interval.

Intermediate resonances in $\Xi_c^+ \rightarrow \Xi^- \pi^+ \pi^+$: In the simulation, the Ξ_c^+ three-body decay is assumed to be entirely non-resonant. However, structure is observed in the Dalitz plot distributions in data. We determine the efficiency for two extreme cases: when the non-resonant contribution is 0% (ε_{res}) and when the non-resonant contribution is 100% ($\varepsilon_{\text{nonres}}$). The overall efficiency is then changed to $(\varepsilon_{\text{res}} + \varepsilon_{\text{nonres}})/2$ with a systematic uncertainty of $(|\varepsilon_{\text{res}} - \varepsilon_{\text{nonres}}|)/2$. This only affects the Ξ_c^+ mode. The effect is approximately 15% at low p^* , dropping to zero at high p^* as the efficiency becomes more uniform across the Dalitz plot.

Finite resolution: The reconstructed p^* distribution is the true p^* distribution convoluted by the resolution function. The resolution varies with p^* , but is typically 15–20 MeV/ c , substantially smaller than the bin size (500 MeV/ c). We therefore neglect this effect.

Admixture of $c\bar{c}$ and $B\bar{B}$ simulation: The angular distributions of Ξ_c' produced in continuum events and in B decays differ, resulting in slightly different efficiencies for the two processes. This is modelled in the simulation. In general it is unambiguous which process dominates in a given p^* interval, but in the p^* interval 1.5–2.0 GeV/ c both may contribute significantly,

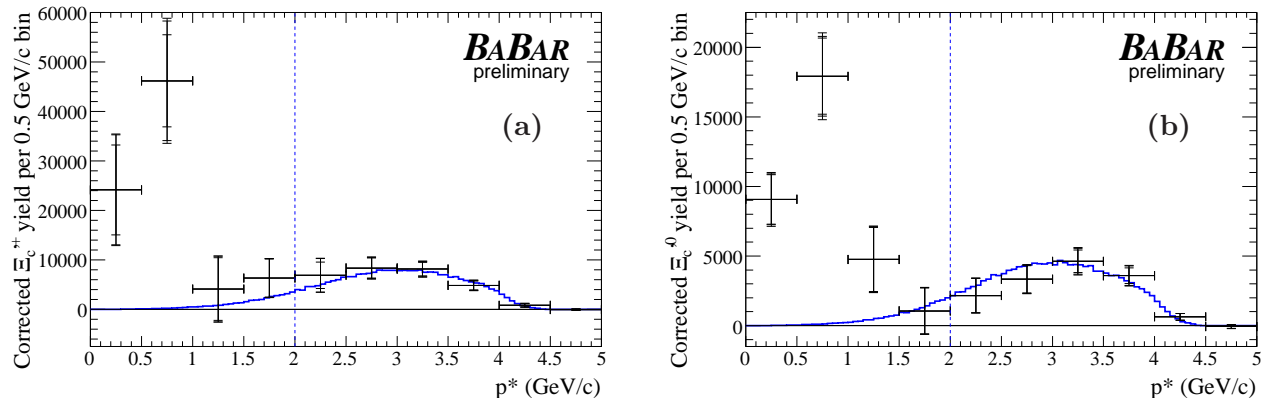


Figure 8: The efficiency-corrected, background-subtracted p^* spectrum for (a) $\Xi_c^{\prime+}$ and (b) $\Xi_c^{\prime0}$. The curve is the simulated continuum distribution described in Section 5; it is fitted to the data for $2.0 < p^* < 4.5$ GeV/ c (indicated by the dashed line).

leading to a slight dependence of the efficiency-corrected yield on the assumed relative production rates. However, the absolute yield in this interval is small and other uncertainties dominate, so we neglect this effect.

After applying these systematic corrections and uncertainties, the p^* spectrum shown in Fig. 8 is obtained. The inner error bars show the statistical uncertainty (both from data and simulation), the middle error bars show the sum in quadrature of the statistical and uncorrelated systematic uncertainties, and the outer error bars (where visible) show the sum of all uncertainties in quadrature.

5 PHYSICS RESULTS

5.1 Production rates

It is clear from Fig. 8 that there is significant Ξ_c' production both in B decays and from the $c\bar{c}$ continuum. We separate the contributions of the two processes as follows:

- B production of Ξ_c' for $p^* > 2.0$ GeV/ c is assumed to be zero.
- Continuum production of Ξ_c' for $p^* > 2.0$ GeV/ c is taken to be the sum of the measured yields in each p^* interval above 2.0 GeV/ c .
- The data between 2.0 GeV/ c and 4.5 GeV/ c are then fitted with a suitable function, described below. The function is extrapolated down to $p^* = 0$ and the integral over the range 0.0–2.0 GeV/ c is taken as the continuum production of Ξ_c' in that momentum range.
- The B production of Ξ_c' below 2.0 GeV/ c is taken to be the sum of the measured yields in each p^* interval below 2.0 GeV/ c less the estimated continuum production in the range 0.0–2.0 GeV/ c .

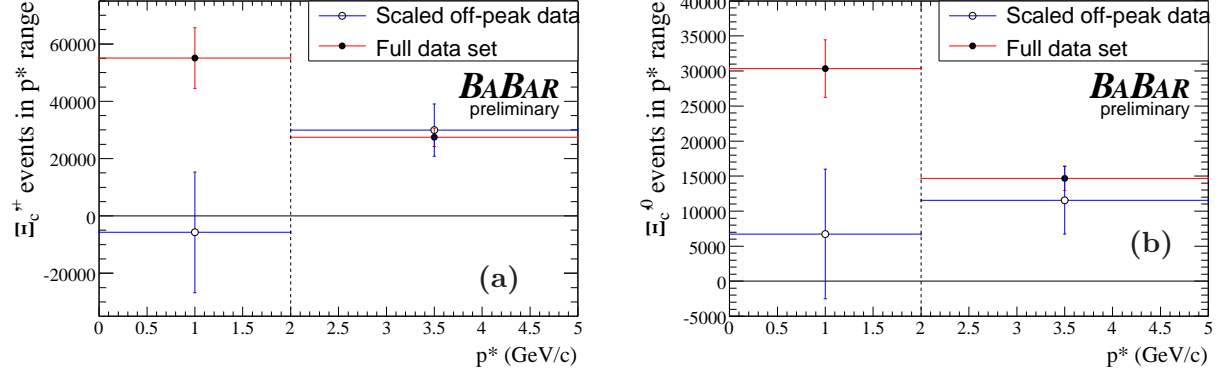


Figure 9: Comparison of the efficiency corrected yields in the off-peak sample with those of the full data set (off-peak and on-peak combined). The off-peak yields have been scaled up to account for the difference in integrated luminosity, and corrected for the small change in the continuum cross-section with \sqrt{s} . Plot (a) shows the $\Xi_c'^+$ and plot (b) shows the $\Xi_c'^0$. Systematic uncertainties and corrections are not included.

The continuum function is based on the Bowler fragmentation model [18], tuned to the global *BABAR* data and implemented within the JETSET [14] generator. Only the amplitude is allowed to float in the fit to the data. The fitted function is shown in Fig. 8. The χ^2/NDF of the fits are 1.2/4 and 1.8/4 for $\Xi_c'^+$ and $\Xi_c'^0$, respectively.

To test the model dependency, we fit the data with a number of other fragmentation models. For these crosschecks, we take the parameterizations to be functions of the scaled momentum x_p . The data above 2.0 GeV/ c are well-described by the Peterson model [19] and by a baryon-specific version of the phenomenological model of Kartvelishvili et al. [20]. The standard deviation of the extracted rates when using these three fragmentation models is quoted as the model-dependent uncertainty:

$$\begin{aligned}
 \Xi_c'^+ \text{ from continuum:} & \quad 32681 \pm 5516 \text{ (exp.)} \pm 4443 \text{ (model)} \\
 \Xi_c'^+ \text{ from } B \text{ decay:} & \quad 77199 \pm 7907 \text{ (exp.)} \pm 4443 \text{ (model)} \\
 \Xi_c'^0 \text{ from continuum:} & \quad 16356 \pm 2509 \text{ (exp.)} \pm 1384 \text{ (model)} \\
 \Xi_c'^0 \text{ from } B \text{ decay:} & \quad 30782 \pm 3088 \text{ (exp.)} \pm 1384 \text{ (model)},
 \end{aligned}$$

where the experimental uncertainties combine both statistical and systematic effects. Excluding the normalization systematic uncertainties, these correspond to a statistical significance for Ξ_c' production in B decays in excess of 12σ for each mode, and a significance for continuum production at $p^* > 2.0$ GeV/ c in excess of 6σ for each mode. As an additional crosscheck, the continuum production for $p^* < 2.0$ GeV/ c is measured in the off-peak data sample alone. This procedure is model-independent (to 2–3%) but has a much larger statistical uncertainty. The results are shown in Fig. 9 and are consistent with the yields quoted above within statistical uncertainties.

Dividing the above yields by twice the total number of $B\bar{B}$ pairs in the data sample, we measure the product branching fractions as:

$$\begin{aligned}
 \mathcal{B}(B \rightarrow \Xi_c'^+ X) \times \mathcal{B}(\Xi_c'^+ \rightarrow \Xi^- \pi^+ \pi^+) &= [1.69 \pm 0.17 \text{ (exp.)} \pm 0.10 \text{ (model)}] \times 10^{-4} \\
 \mathcal{B}(B \rightarrow \Xi_c'^0 X) \times \mathcal{B}(\Xi_c'^0 \rightarrow \Xi^- \pi^+) &= [0.67 \pm 0.07 \text{ (exp.)} \pm 0.03 \text{ (model)}] \times 10^{-4}.
 \end{aligned}$$

Comparing the second measurement with a previous *BABAR* result [7],

$$\mathcal{B}(B \rightarrow \Xi_c^0 X) \times \mathcal{B}(\Xi_c^0 \rightarrow \Xi^- \pi^+) = [2.11 \pm 0.19 \text{ (stat.)} \pm 0.25 \text{ (sys.)}] \times 10^{-4},$$

we observe that approximately one third of Ξ_c^0 produced in B decays come from $\Xi_c^{\prime 0}$ decays.

Correcting for the $1/s$ scaling of the continuum cross-section for data taken at $\sqrt{s} = 10.54$ GeV and taking into account the 1.5% systematic uncertainty on the integrated luminosities quoted in Section 2, the cross-sections at $\sqrt{s} = 10.58$ GeV are:

$$\begin{aligned} \sigma(e^+e^- \rightarrow \Xi_c^{\prime +} X) \times \mathcal{B}(\Xi_c^+ \rightarrow \Xi^- \pi^+ \pi^+) &= 141 \pm 24 \text{ (exp.)} \pm 19 \text{ (model) fb} \\ \sigma(e^+e^- \rightarrow \Xi_c^{\prime 0} X) \times \mathcal{B}(\Xi_c^0 \rightarrow \Xi^- \pi^+) &= 70 \pm 11 \text{ (exp.)} \pm 6 \text{ (model) fb.} \end{aligned}$$

Comparing this with a previous *BABAR* result [7]:

$$\sigma(e^+e^- \rightarrow \Xi_c^0 X) \times \mathcal{B}(\Xi_c^0 \rightarrow \Xi^- \pi^+) = 388 \pm 39 \text{ (stat.)} \pm 41 \text{ (sys.) fb}$$

we observe that about 18% of Ξ_c^0 produced in the continuum come from a $\Xi_c^{\prime 0}$.

5.2 Helicity angle distribution

The quark-model predicts $J^P = \frac{1}{2}^+$ for Ξ_c^{\prime} , Ξ_c and Ξ^- . Under this assumption, the helicity angle distribution for the decay processes studied should be flat in the cosine of the helicity angle, $\cos \theta_h$, where θ_h defined as is the angle between the Ξ^- direction in the Ξ_c rest frame and the Ξ_c direction in the Ξ_c^{\prime} rest frame. If the Ξ_c^{\prime} has $J = \frac{3}{2}$, the angular distribution is of the form $c_1 + c_2 \cos^2 \theta_h$ where c_1 and c_2 are unknown parameters and c_2 may be zero. In general the distribution for higher spins is a higher-order polynomial—but the distribution may be flat if the higher-order coefficients are zero. Therefore, a non-flat distribution in the data would exclude $J = \frac{1}{2}$, but a flat distribution would not exclude $J > \frac{1}{2}$.

The method used to measure the helicity angle distribution in the data is similar to the one used for the p^* spectrum: we divide the data into six slices of $\cos \theta_h$ and fit the mass spectrum in each slice. A p^* threshold of 2.5 GeV/ c is applied throughout to improve the signal-to-background ratio. After correcting for efficiency, the distributions are fitted with two functions: first, a flat distribution:

$$f_0(\cos \theta_h) = \alpha \tag{3}$$

and second, a symmetric quadratic:

$$f_0(\cos \theta_h) = \alpha \left(1 + \beta \cos^2 \theta_h \right). \tag{4}$$

Separate fits to each mode in the data are performed and the fit results are shown in Table 1. The data are clearly consistent with being flat (χ^2/NDF less than unity). The fitted quadratic parameters β are consistent with zero, though with large statistical uncertainties. Since the two modes should have identical helicity distributions, we weight them according to their statistical precision and combine them—this is shown in Fig. 10 and the fit results are given in Table 1. The data are still fit well by a flat distribution, though with a somewhat reduced χ^2 probability (20%). From this we conclude that the data are consistent with the predicted $J = \frac{1}{2}$ but that higher spins cannot be excluded.

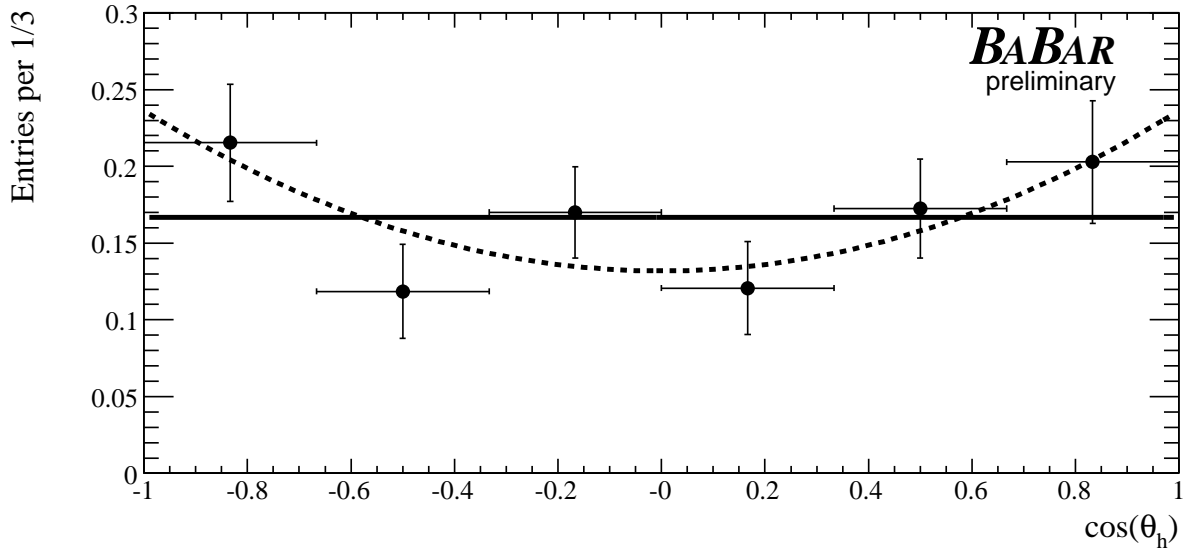


Figure 10: Fits to efficiency-corrected helicity distributions for data with $p^* > 2.5$ GeV/ c . The plot shows the normalized, weighted sum of the $\Xi_c^{\prime+}$ and $\Xi_c^{\prime0}$ distributions. The solid line assumes a flat helicity distribution, whereas for the dashed line a quadratic term is added.

Table 1: Results of fits to efficiency-corrected helicity distributions. The χ^2 goodness-of-fit and the number of degrees of freedom are given for the flat and quadratic distributions given in Eq. 3 and 4, along with the fitted parameter β from the quadratic distribution. The results are given for the $\Xi_c^{\prime+}$ and $\Xi_c^{\prime0}$ samples individually, and for a weighted sum of the two samples.

	$\Xi_c^{\prime+}$	$\Xi_c^{\prime0}$	Weighted Sum
χ^2/NDF for flat	4.0/5 (55%)	4.4/5 (50%)	7.3/5 (20%)
χ^2/NDF for quadratic	2.7/4 (61%)	1.3/4 (87%)	3.0/4 (55%)
β for quadratic	0.63 ± 0.68	1.04 ± 0.82	0.79 ± 0.52

6 SUMMARY

We have confirmed the CLEO observation of the $\Xi_c^{\prime+}$ and $\Xi_c^{\prime0}$ states from the $c\bar{c}$ continuum. In addition, we found that B mesons decay at a substantial rate to $\Xi_c^{\prime+}$ and $\Xi_c^{\prime0}$. This is the first observation of such decays; the statistical significance is in excess of 12σ for each mode. We have measured the production rates of Ξ_c^{\prime} from B decays (expressed as a branching fraction) and from the $c\bar{c}$ continuum (expressed as a cross-section); in both cases, the absolute rate is scaled by the unknown absolute Ξ_c branching fraction. We have measured the angular distribution of $\Xi_c^{\prime} \rightarrow \Xi_c \gamma$ decays and found it to be consistent with the prediction for $J^P = \frac{1}{2}^+$. However, higher spins cannot be ruled out.

7 ACKNOWLEDGMENTS

We are grateful for the extraordinary contributions of our PEP-II colleagues in achieving the excellent luminosity and machine conditions that have made this work possible. The success of this project also relies critically on the expertise and dedication of the computing organizations that support *BABAR*. The collaborating institutions wish to thank SLAC for its support and the kind hospitality extended to them. This work is supported by the US Department of Energy and National Science Foundation, the Natural Sciences and Engineering Research Council (Canada), Institute of High Energy Physics (China), the Commissariat à l’Energie Atomique and Institut National de Physique Nucléaire et de Physique des Particules (France), the Bundesministerium für Bildung und Forschung and Deutsche Forschungsgemeinschaft (Germany), the Istituto Nazionale di Fisica Nucleare (Italy), the Foundation for Fundamental Research on Matter (The Netherlands), the Research Council of Norway, the Ministry of Science and Technology of the Russian Federation, Ministerio de Educación y Ciencia (Spain), and the Particle Physics and Astronomy Research Council (United Kingdom). Individuals have received support from the Marie-Curie IEF program (European Union) and the A. P. Sloan Foundation.

References

- [1] K. Maltman and N. Isgur, Phys. Rev. D **22**, 1701 (1980).
- [2] Particle Data Group, S. Eidelman *et al.*, Phys. Lett. **B592**, 1 (2004).
- [3] The *BABAR* Collaboration, B. Aubert *et al.*, hep-ex/0606037, submitted to Phys. Rev. Lett..
- [4] The CLEO Collaboration, C. P. Jessop *et al.*, Phys. Rev. Lett. **82**, 492 (1999).
- [5] The Belle Collaboration, N. Gabyshev *et al.*, hep-ex/0508015, submitted to Phys. Rev. Lett..
- [6] The Belle Collaboration, R. Chistov *et al.*, hep-ex/0510074, submitted to Phys. Rev. Lett..
- [7] The *BABAR* Collaboration, B. Aubert *et al.*, Phys. Rev. Lett. **95**, 142003 (2005).
- [8] The *BABAR* Collaboration, B. Aubert *et al.*, Phys. Rev. D **70**, 091106 (2004).
- [9] The *BABAR* Collaboration, B. Aubert *et al.*, hep-ex/0606026, submitted to Phys. Rev. D.
- [10] H. Y. Cheng, hep-ph/0603003.

- [11] M. Z. Wang *et al.*, Phys. Lett. B **617**, 141 (2005).
- [12] The *BABAR* Collaboration, B. Aubert *et al.*, Phys. Rev. D **72**, 051101 (2005).
- [13] The *BABAR* Collaboration, B. Aubert *et al.*, Nucl. Instrum. Methods **A479**, 1-116 (2002).
- [14] T. Sjostrand *et al.*, Comput. Phys. Commun. **135**, 238 (2001).
- [15] S. Agostinelli *et al.*, Nucl. Instr. Methods Phys. Res., Sect. A **506**, 250 (2003).
- [16] The *BABAR* Collaboration, P.F. Harrison and H.R. Quinn ed., SLAC-R-0504.
- [17] F. James and M. Roos, Comput. Phys. Commun. **10**, 343 (1975).
- [18] M.G. Bowler, Z. Phys. **C11** (1981) 169.
- [19] C. Peterson, D. Schlatter, I. Schmitt and P.M. Zerwas, Phys. Rev. **D27** (1983) 105.
- [20] V.G. Kartvelishvili and A.K. Likhoded, Sov. J. Nucl. Phys **29** (1979) 390.

Appendix

A Lineshape parameterizations

A.1 Triple Gaussian function

The lineshape function $f(\Delta m)$ is parameterized as follows:

$$f(\Delta m) = N(1 - f_2 - f_3)G(\Delta m; \mu_1, \sigma_1) + N f_2 G(\Delta m; \mu_1 + \Delta\mu_2, \sigma_2) + N f_3 G(\Delta m; \mu_1 + \Delta\mu_3, \sigma_3) \quad (5)$$

where $G(x; \mu, \sigma)$ is a Gaussian function of unit area with mean μ and width σ . The nine parameters are then interpreted as follows:

N	Total fitted yield
f_2	Fraction of yield in second Gaussian function
f_3	Fraction of yield in third Gaussian function
μ_1	Signal mass
$\Delta\mu_2$	Mean of second Gaussian function with respect to the signal mass
$\Delta\mu_3$	Mean of third Gaussian function with respect to the signal mass
σ_1	Width of first Gaussian function
σ_2	Width of second Gaussian function
σ_3	Width of third Gaussian function

When fitting simulated events to determine the lineshape, all nine parameters are allowed to vary independently. In order to improve fit convergence, the following bounds are placed on the variation of the parameters:

N	No bounds
f_2	No bounds
f_3	No bounds
μ_1	Limited to $(-5, +5)$ MeV/ c^2 relative to the true mass
$\Delta\mu_2$	Limited to $(-15, +5)$ MeV/ c^2 relative to μ_1
$\Delta\mu_3$	Limited to $(-35, -5)$ MeV/ c^2 relative to μ_1
σ_1	Limited to $(0, 10)$ MeV/ c^2
σ_2	Limited to $(4, 20)$ MeV/ c^2
σ_3	Limited to $(20, 100)$ MeV/ c^2

A.2 Alternative lineshape parameterization

The following functional form was also used as a cross-check and to determine the systematic uncertainty due to the signal lineshape:

$$f(x) = A_p \times \begin{cases} \exp \left[\frac{4\xi\sqrt{\xi^2+1}\cdot(x-x_1)\ln 2}{h_p\cdot(\sqrt{\xi^2+1}-\xi)^2 \ln(\sqrt{\xi^2+1}+\xi)} + \rho_1 \cdot \left(\frac{x-x_1}{x_p-x_1} \right)^2 - \ln 2 \right] & , \quad x < x_1, \\ \exp \left[-\ln 2 \cdot \left[\frac{\ln(1+4\xi\sqrt{\xi^2+1}\cdot\frac{x-x_p}{h_p})}{\ln(1+2\xi^2-2\xi\sqrt{\xi^2+1})} \right]^2 \right] & , \quad x_1 < x < x_2, \\ \exp \left[-\frac{4\xi\sqrt{\xi^2+1}\cdot(x-x_2)\ln 2}{h_p\cdot(\sqrt{\xi^2+1}+\xi)^2 \ln(\sqrt{\xi^2+1}+\xi)} + \rho_2 \cdot \left(\frac{x-x_2}{x_p-x_2} \right)^2 - \ln 2 \right] & , \quad x > x_2. \end{cases}$$

where

$$\begin{aligned}
 x_1 &\equiv x_p + \frac{h_p}{2} \left[\frac{\xi}{\sqrt{\xi^2 + 1}} - 1 \right] \\
 x_2 &\equiv x_p + \frac{h_p}{2} \left[\frac{\xi}{\sqrt{\xi^2 + 1}} + 1 \right].
 \end{aligned}$$

Of the six parameters A_p controls the amplitude, x_p controls the peak position, h_p controls the width, ξ controls the asymmetry in the central region, ρ_1 controls the lower tail, and ρ_2 controls the upper tail.

B Individual mass spectra

The fitted mass spectra for individual p^* intervals are shown in Fig. 11 and 12 for $\Xi_c'^+$ and $\Xi_c'^0$, respectively.

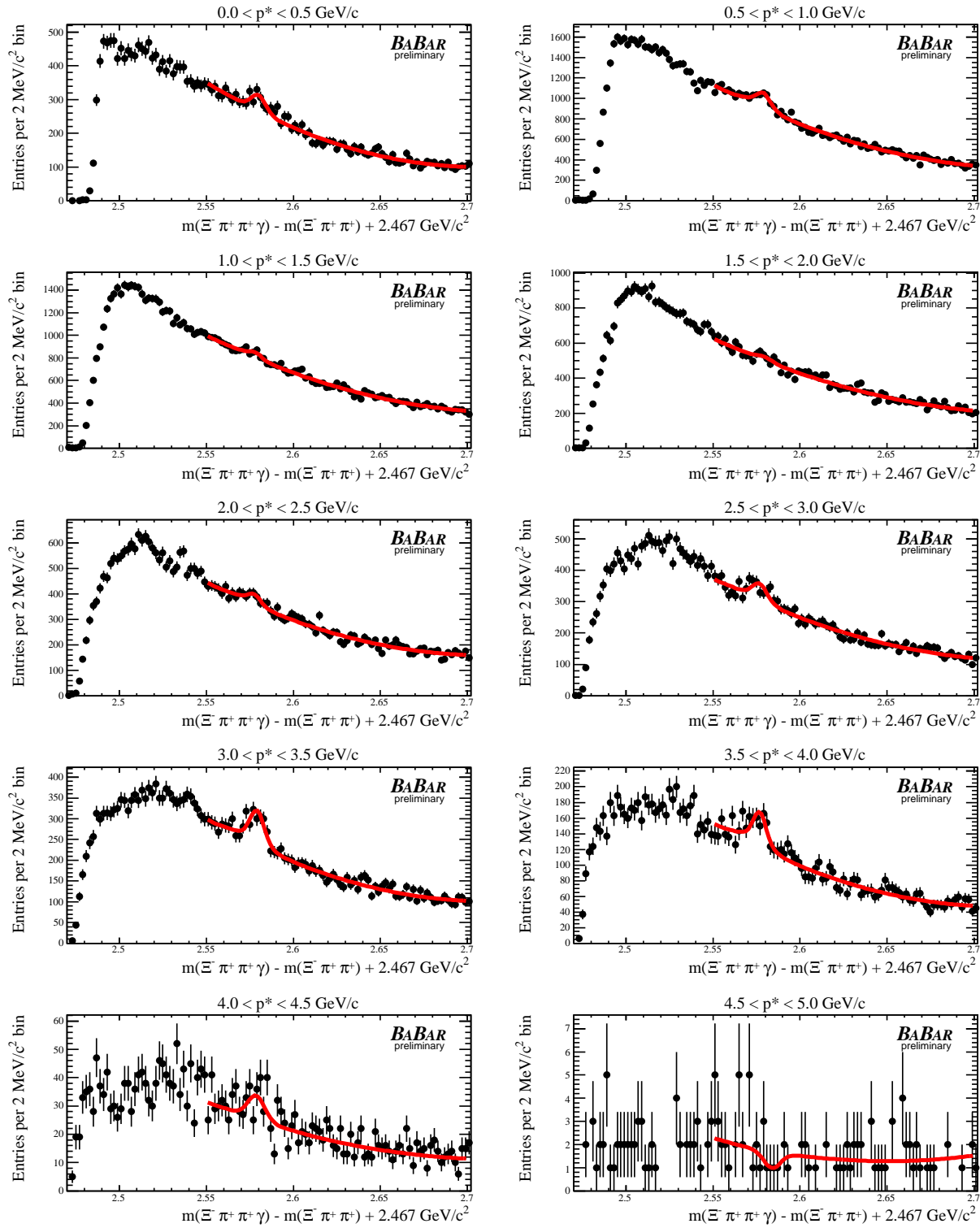


Figure 11: The $\Xi_c^+ \gamma$ invariant mass spectra for each of the ten p^* intervals used. The points show data from the Ξ_c^+ signal mass region (within 3σ of the central value).

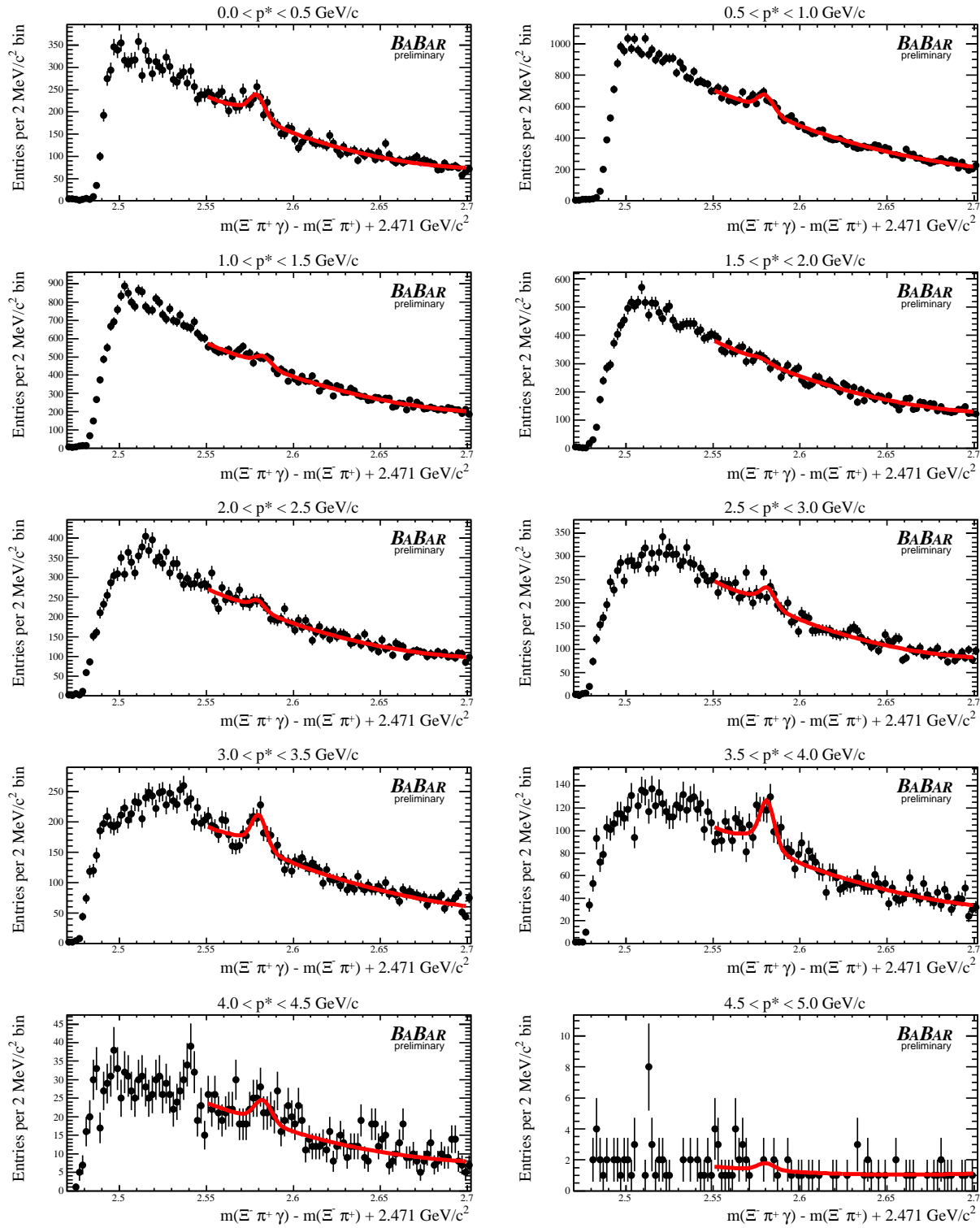


Figure 12: The $\Xi_c^0 \gamma$ invariant mass spectra for each of the ten p^* intervals used. The points show data from the Ξ_c^0 signal mass region (within 3σ of the central value).